Detection of Rain in Tropical Cyclones by Underwater Ambient Sound

ZHONGXIANG ZHAO[a,b] AND ERIC A. D'ASARO[a,b]

[a] *Applied Physics Laboratory, University of Washington, Seattle, Washington*
[b] *School of Oceanography, University of Washington, Seattle, Washington*

(Manuscript received 17 July 2022, in final form 19 June 2023, accepted 23 June 2023)

ABSTRACT: Rain in tropical cyclones is studied using eight time series of underwater ambient sound at 40–50 kHz with wind speeds up to 45 m s^{-1} beneath three tropical cyclones. At tropical cyclone wind speeds, rain- and wind-generated sound levels are comparable, and therefore rain cannot be detected by sound level alone. A rain detection algorithm that is based on the variations of 5–30-kHz sound levels with periods longer than 20 s and shorter than 30 min is proposed. Faster fluctuations (<20 s) are primarily due to wave breaking, and slower ones (>30 min) are due to overall wind variations. Higher-frequency sound (>30 kHz) is strongly attenuated by bubble clouds. This approach is supported by observations that, for wind speeds < 40 m s^{-1}, the variation in sound level is much larger than that expected from observed wind variations and is roughly comparable to that expected from rain variations. The hydrophone results are consistent with rain estimates by the Tropical Rainfall Measuring Mission (TRMM) satellite and with Stepped-Frequency Microwave Radiometer (SFMR) and radar estimates by surveillance flights. The observations indicate that the rain-generated sound fluctuations have broadband acoustic spectra centered around 10 kHz. Acoustically detected rain events usually last for a few minutes. The data used in this study are insufficient to produce useful estimation of rain rate from ambient sound because of limited quantity and accuracy of the validation data. The frequency dependence of sound variations suggests that quantitative rainfall algorithms from ambient sound may be developed using multiple sound frequencies.

SIGNIFICANCE STATEMENT: Rain is an indispensable process in forecasting the intensity and path of tropical cyclones. However, its role in the air–sea interaction is still poorly understood, and its parameterization in numerical models is still in development. In this work, we analyzed sound measurements made by hydrophones on board Lagrangian floats beneath tropical cyclones. We find that wind, rain, and breaking waves each have distinctive signatures in underwater ambient sound. We suggest that the air–sea dynamic processes in tropical cyclones can be explored by listening to ambient sound using hydrophones beneath the sea surface.

KEYWORDS: Rainbands; Tropical cyclones; Air–sea interaction; Acoustic measurements/effects; Satellite observations

1. Introduction

Rain is an inherent element of tropical cyclones and plays an important role in the air–sea interaction in tropical cyclones. Rain damps short surface waves and thus modifies the air–sea drag coefficient. Rain within tropical cyclones forms a layer of freshwater at the sea surface, which strengthens upper-ocean stratification, and affects the air–sea flux in tropical cyclones (Steffen and Bourassa 2018, 2020). At landfall, strong wind and heavy rain both pose threat to human lives and properties. Accurate and timely prediction of rain associated with tropical cyclones has significant societal impacts. For example, Hurricane Harvey (2017) brought heavy rain and caused disastrous flooding in Texas and Louisiana (Emanuel 2017; Valle-Levinson et al. 2020). Recent studies suggest that rain associated with tropical cyclones may increase in the future, because more moisture is present in tropical cyclones over warmer oceans (van Oldenborgh et al. 2017; Risser and Wehner 2017). Rain has an important effect on remote sensing of wind speed in tropical cyclones (e.g., microwave and infrared radiometers), because it absorbs outgoing radiation from the ocean surface (Jiang et al. 2006; Klotz and Uhlhorn 2014; Walsh et al. 2014).

Despite its importance, measuring rain is difficult, especially in tropical cyclones. Traditional rain gauges do not work well in such a harsh environment. Surveillance aircraft flying into tropical cyclones estimate rain rate from microwave radiation and with active radars. The Tropical Rainfall Measuring Mission (TRMM) satellite and the Global Precipitation Measurement (GPM) consortium may provide global coverage (Kummerow et al. 1998; Hou et al. 2014). However, these observations are significantly limited by the spatiotemporal coverage of surveillance flights and satellites. In this paper, we explore the detection of rain by underwater ambient sound to better understand the feasibility of developing an underwater acoustic technique for estimating rain rate in tropical cyclones. It is a potentially powerful and low-cost approach that can be integrated with a wide variety of subsurface platforms (e.g., Lagrangian float, sea glider, and Argo float). The underwater acoustic technique may be useful in the study of air–sea dynamic processes in tropical cyclones.

Rain generates sound when raindrops hit the ocean surface and entrain bubbles (Nystuen and Farmer 1987; Nystuen et al. 1993; Nystuen 2001). A new bubble radiates sound at its resonance frequency f following

$$f = \frac{1}{2\pi a}\sqrt{\frac{3\gamma P}{\rho}}, \tag{1}$$

Corresponding author: Zhongxiang Zhao, zzhao@apl.uw.edu

DOI: 10.1175/JTECH-D-22-0078.1

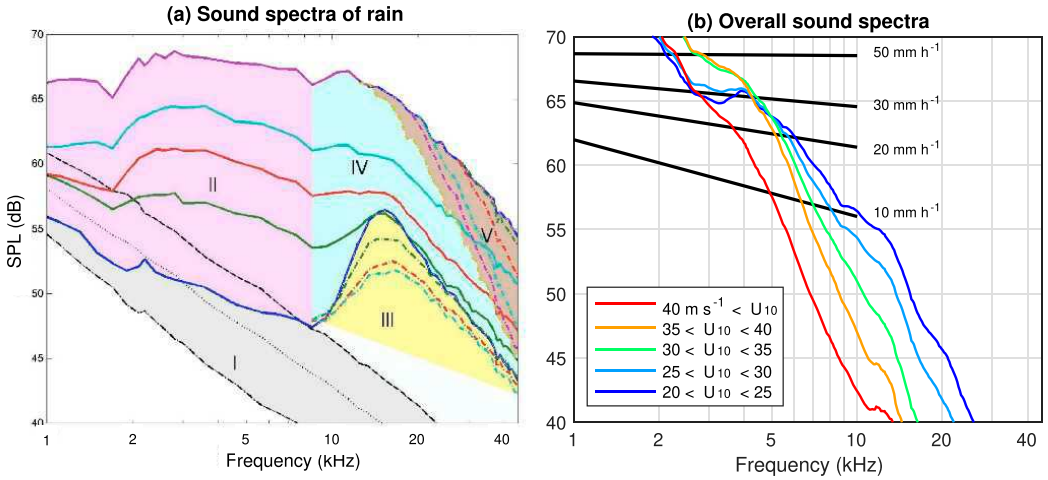

FIG. 1. Spectra of underwater ambient sound: (a) Sound spectra of rain, taken from Fig. 5 in Ma et al. (2005). The spectra have five distinctive sections (color coded)—(I) wind-only (<14 m s^{-1}), (II) large raindrops, (III) small raindrops, (IV) both small and large raindrops, and (V) attenuation by rain-generated bubble clouds. Wind-dependent spectral portions are indicated by dash–dotted lines. These five sections may overlap. (b) Sound spectra at high winds (with or without rain). Colored lines are from Fig. 3 in Zhao et al. (2014). The sound level > 3 kHz decreases with increasing wind speed, because of attenuation by bubble clouds. The black lines indicate the empirical algorithm of rain rate in the low-wind condition developed by Ma et al. (2005).

where a is the bubble radius, γ is the bubble surface tension, P is ambient pressure, and ρ is water density. The sound frequency is inversely proportional to the bubble radius. The sound signature of rain is determined by a variety of factors such as rain rate, the size distribution of raindrops, terminal speed, wind speed, subsurface bubble cloud, and the state of the ocean surface (Scrimger et al. 1987; Nystuen 1996; Ma et al. 2005). The sound spectra of rain at low winds have been well studied (Medwin et al. 1992; Nystuen and Medwin 1995; Nystuen 1996). Ma et al. (2005) obtained the sound spectra created by different types of rainfall at winds < 14 m s^{-1} (Fig. 1a). In convective rain, large and very large raindrops with radii greater than 2.2 mm generate spectra with a peak ranging 1–10 kHz (Fig. 1a, II). In drizzle and light rain, small raindrops with radius ranging from 0.8 to 1.2 mm create sound spectra with a peak ranging over 13–25 kHz (Fig. 1a, III). In most cases, rain contains mixed drop sizes and thus causes sound spectra louder in frequency ranging 2–35 kHz (Fig. 1a, IV). Extremely heavy rain may form bubble clouds in the surface layer, which attenuate sound from newly generated bubbles and decreases sound level (Fig. 1a, V). Based on simultaneous rain and hydrophone measurements, Ma et al. (2005) developed an empirical algorithm to estimate rain rate (RR) following

$$\mathrm{RR} = 10^{(\mathrm{SPL}_{5k} - 42.4)/15.4}, \tag{2}$$

where SPL_{5k} is the 5-kHz sound pressure level (Fig. 1b, black lines).

Rain is detectable in underwater ambient sound at low winds, because rain-generated sound is much louder than wind-generated sound (Fig. 1a, I). However, this technique cannot be extended to the high-wind regime, because the wind- and rain-generated sound levels become comparable (Fig. 1b). According to the empirical relation between wind speed U_{10} and 8-kHz sound pressure level SPL_{8k} developed by Vagle et al. (1990),

$$U_{10} = (10^{\mathrm{SPL}_{8k}/20} + 104.5)/53.91, \tag{3}$$

the 8-kHz sound increases from 44.2 dB at 5 m s^{-1} to 63.5 dB at 30 m s^{-1}, which is close to the sound level caused by rain of 20–30 mm h^{-1} (Fig. 1b).

Rain-induced sound remains louder than the wind-generated sound at intermediate frequencies around 10 kHz. However, sound from both wind and rain is attenuated by bubble clouds at high winds. Previous studies have shown that bubble clouds start to appear at wind speed of 8 m s^{-1} and permanently exist in the surface layer for wind >15 m s^{-1}. Bubble clouds absorb newly generated sound around their resonant frequencies (Farmer and Lemon 1984; Nystuen 2001; Zhao et al. 2014). For example, Fig. 1b shows that the sound spectra at high winds >20 m s^{-1} are attenuated by bubble clouds. The hydrophone measurements contain sound from all sources including wind and rain. The lower-frequency (<1 kHz) sound level increases with increasing wind. However, the higher-frequency (>5 kHz) sound level decreases with increasing wind due to bubble absorption. Above 30 m s^{-1}, bubbles reduce the sound level to below the noise level of the hydrophone (≈30 dB) for frequencies >20 kHz. Thus, for increasing wind speed, there is only a narrow range of acoustic frequencies where the rain signal rises well above the wind signal and the bubble attenuation is still weak so that there is measurable sound. However, at hurricane wind speeds, this range is small or nonexistent.

Zhao et al. (2014) described the variation of sound levels from 40 to 50 kHz measured by Lagrangian floats air-deployed into three tropical cyclones with wind speeds ranging from 15 to 50 m s^{-1}, attributing most of the slow variations to wind speed.

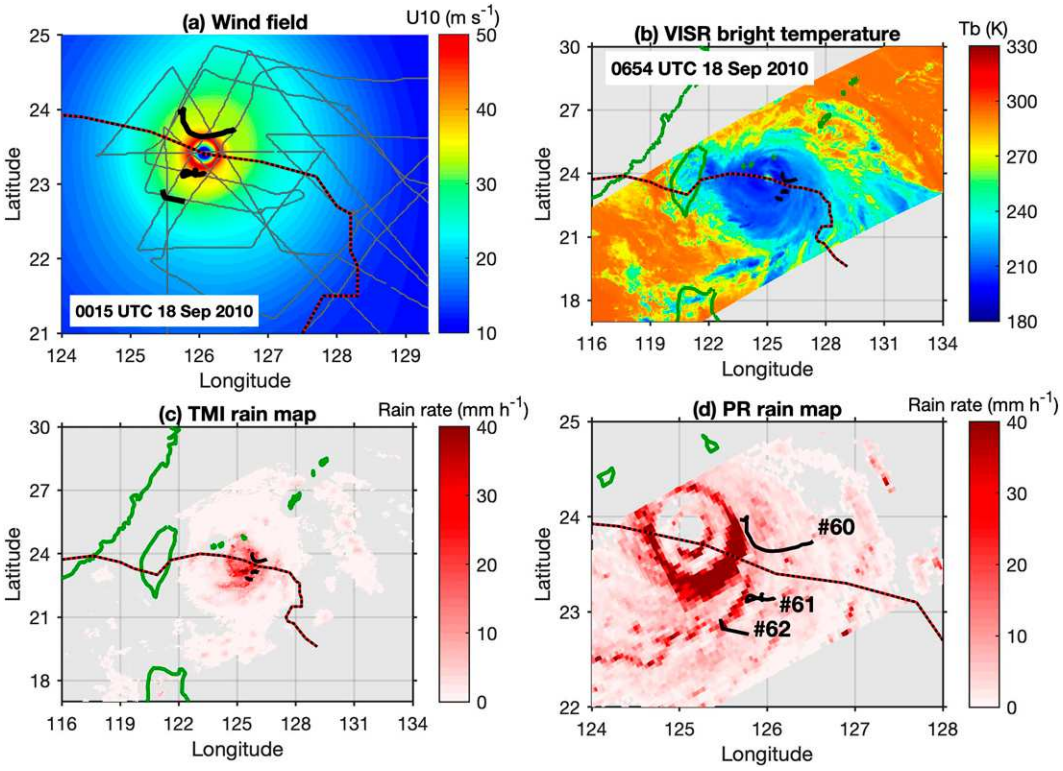

FIG. 2. Field experiment in Typhoon Fanapi: (a) Wind field constructed using aircraft observations around 0015 UTC 18 Sep 2010. The gray lines are the ground tracks of four surveillance flights of this storm plotted relative to storm center. (b) TRMM Visible and Infrared Scanner (VIRS) brightness temperature. (c) TRMM Microwave Imager (TMI) rain map. (d) Precipitation radar (PR) rain map. In (a)–(d), the black lines indicate the trajectories of floats 60–62 and the dashed lines indicate the path of Fanapi. Note that the aircraft flight and wind field were about 7 h earlier than the TRMM observations.

Here, we use the same data to separate the rain signal from the wind signal. We decompose underwater ambient sound into three components based on the sound variations over various time scales. We find that minute-scale sound fluctuations are mainly caused by intermittent rain. It is confirmed by comparing with aircraft and satellite observations, although simultaneous ground-truth measurements are sparse and noisy. This yields a simple method to detect rain. However, more simultaneous measurements are needed to develop a reliable algorithm for quantitatively estimating rain rate at high winds.

The rest of this paper is arranged as follows. Section 2 introduces the field experiments. Section 3 describes how to decompose underwater ambient sound and detect rain in sound fluctuation. Section 4 confirms the identified rain events by spatiotemporally matched satellite and aircraft observations. Section 5 presents rain features in tropical cyclones observed using underwater ambient sound. Section 6 contains a summary.

2. Field experiments

Underwater ambient sound measurements were made in three tropical cyclones: Hurricane Gustav (2008) in the Gulf of Mexico, and Typhoons Fanapi (September 2010) and Megi (October 2010) in the western Pacific Ocean as part of the Impact of Typhoons on the Ocean in the Pacific (ITOP) program (D'Asaro et al. 2011, 2014). Measurements were made from eight Lagrangian floats, each equipped with one hydrophone, air-deployed ahead of these storms by WC-130J aircraft operated by the U.S. Air Force Reserve 53rd Weather Reconnaissance squadron "Hurricane Hunters." Floats 50 and 51 were in Gustav, 60, 61, and 62 in Fanapi, and 66, 67, and 68 in Megi (Zhao et al. 2014). These aircraft flights also mapped the surface wind field and rain rate using onboard instruments. After the storm passage, the Lagrangian floats were recovered by a research vessel. Float positions were determined by interpolating between a few GPS positions taken during the storm passage guided by time-integrated velocity measurements from Electromagnetic Autonomous Profiling Explorer (EM-APEX) floats deployed at the same time as the Lagrangian floats (Sanford et al. 2011; Hsu et al. 2017). For example, Fig. 2a shows the trajectories of floats 60, 61, and 62 (black lines) and the tracks of four aircraft surveillance flights relative to the storm (gray lines) over the four consecutive days preceding landfall on Taiwan on 19 September 2010. These measurements have been used to study the drag coefficient and ocean responses during the same storms (e.g., Pun et al. 2011; Lin et al. 2013; Mrvaljevic et al. 2013; Zhao et al. 2014; Hsu et al. 2017, 2019; Zhou et al. 2022). For each surveillance flight, one wind field was

constructed as described in Zhao et al. (2014). Figure 2a shows the wind field constructed using aircraft observations on 18 September 2010. For Hurricane Gustav, wind fields were produced using the operational HWIND program (Powell et al. 1998, 2010).

a. Hydrophone measurements

During the passage of tropical cyclones, the hydrophone switched between the work and sleep modes every 30 min due to limited data storage. In the work mode, the hydrophones sampled underwater ambient sound twice per second. The sound measurements thus are in 30-min segments. There are 39 (50), 38 (51), 60 (60), 56 (61), 56 (62), 55 (66), 53 (67), and 51 (68) segments (float serial numbers are in parentheses), respectively, giving a total of 408 data segments and about 190 h of sound measurements. Each raw time series has been Fourier transformed to obtain a power spectrum from 40 to 50 kHz, with a spectral resolution of 40 Hz. The sound pressure level (SPL) in decibels (dB) is defined as

$$\mathrm{SPL} = 20\log(P/P_{\mathrm{ref}}), \tag{4}$$

where P is the hydrophone-measured sound pressure and P_{ref} is the reference pressure 1 $\mu\mathrm{Pa}^2\ \mathrm{Hz}^{-2}$. The hydrophones were intercalibrated in laboratory before and after the deployments and agreed with each other, with an RMS difference of 1–2 dB (Zhao et al. 2014).

Each Lagrangian float carried a variety of instruments including a pumped conductivity, temperature, and depth (CTD) sensor, a pumped gas tension device (GTD), a motor to control drogue, and another motor to control the float's buoyancy (D'Asaro et al. 2011, 2014). These instruments generated noise of different temporal and spectral features. Sound measurements contaminated by noise were removed as described in Zhao et al. (2014). One exception is GTD, which ran for 90% of the time for floats 50 and 51 (Gustav) and 66, 67, and 68 (Megi) and caused significant contamination on the <5-kHz sound data. However, the >5-kHz sound measurements are not affected by the GTD noise, and thus kept for rain detection in this study (using 5–30-kHz sound).

b. Aircraft wind and rain estimates

The Air Force WC-130J and the NOAA WP-3D collectively conducted four flights in Typhoon Fanapi, three in Typhoon Megi, and four flights in Hurricane Gustav. During each flight a nadir-looking Stepped-Frequency Microwave Radiometer (SFMR) estimated rain rate and wind speed using passive microwave radiation from the ocean surface (Uhlhorn and Black 2003; Uhlhorn et al. 2007). The wind and rain estimates used in this study are 30-s-averaged values. The 30-s temporal resolution is sufficient to resolve minute-scale variations, which will be compared with minute-scale variations in sound. However, the 30-s-averaged measurements may miss high-frequency variations. Figure 3 gives the estimated wind speed and rain rate near the center of Fanapi during a 4.5-h flight on 18 September 2010. Figure 3a shows the flight pattern. Figures 3b and 3c present time series of wind speed and rain rate. They show a narrow inner band of high wind and heavy rain at the eyewall. There are also several outer rainbands. Combining data from all eyewall penetrations, the result suggests that wind speed and rain rate are closely correlated (Fig. 3d), as previously observed by Houze et al. (2006). Figure 3e presents the mean and standard deviation of wind speeds as a function of distance from the storm center in 10-km bins. For a flight speed of 90 m s^{-1}, a 10-km bin is equivalent to 1.7 min in time, which just meets our need to study the minute-scale variations in rain and wind (section 4e). The wind variations of 1–2 m s^{-1} are relatively small in comparison with the mean, and the rain variations are as large as 5 mm h^{-1} and are comparable to the mean. This suggests that rain is more intermittent than wind over minute-scale time scales.

In the same format, Fig. 4 gives the SFMR-estimated wind speed and rain rate in Typhoon Megi on 16 October 2010. Figure 4a shows that the wind field of Megi is azimuthally asymmetric (unlike Fanapi), which may lead to larger wind variation in 10-km bins. However, Fig. 4 shows similar features as in Fig. 3. For the same reason, Fig. 4e also suggests that rain is much more intermittent than wind. This feature will be used to distinguish the sound signatures of rain (section 3).

The NOAA WP-3D aircraft also routinely estimates rain rate using its tail and lower-fuselage radars. These estimates correlate well with SFMR when these instruments are properly calibrated (Jiang et al. 2006). The lower-fuselage radar yields a time series of reflectivity images (dBZ). Its sampling rate is two images per minute. Each image is created using measurements in one round made by the rotating antenna. The advantage of the active radar (relative to SFMR) is its large spatial coverage of about 200 km in radius. In the past, lower-fuselage radar images have been used to study the spatial structure of tropical cyclones (e.g., Rogers and Uhlhorn 2008). The radar images were downloaded from the website of the NOAA/AOML/Hurricane Research Division. In this study, we use them to confirm an acoustically detected rain event (section 4d).

c. TRMM satellite rain estimates

The TRMM satellite measures rainfall and energy exchange in tropical and subtropical regions between 35°S and 35°N (Kummerow et al. 1998). The primary rainfall instruments on board TRMM are the active Precipitation Radar (PR), the passive TRMM Microwave Imager (TMI), and the Visible and Infrared Scanner (VIRS). Precipitation inferred from the VIRS brightness temperature is less reliable; however, it is useful to combine with other satellites for long-term observations of precipitation. The VIRS temperature field covers a wide swath of 720 km. The TMI rain estimates have a swath of 878 km and a spatial resolution of ~5 km. The PR estimates have a swath that is approximately 247 km wide and a spatial resolution of 0.25–0.3 km. Jiang et al. (2011) compiled a database of the tropical precipitation, cloud, and convective cell feature (TCPF). The TCPF catalogs the TRMM estimates using an event-based format and facilitates the use of TRMM's multisensor observations.

The TRMM observations in Typhoon Fanapi are demonstrated in Fig. 2. Figure 2b shows brightness temperature measured by the VIRS. Figures 2c and 2d present the rain maps estimated by the TMI and PR, respectively. The TMI map cannot clearly resolve the spatial distribution of rain, due to

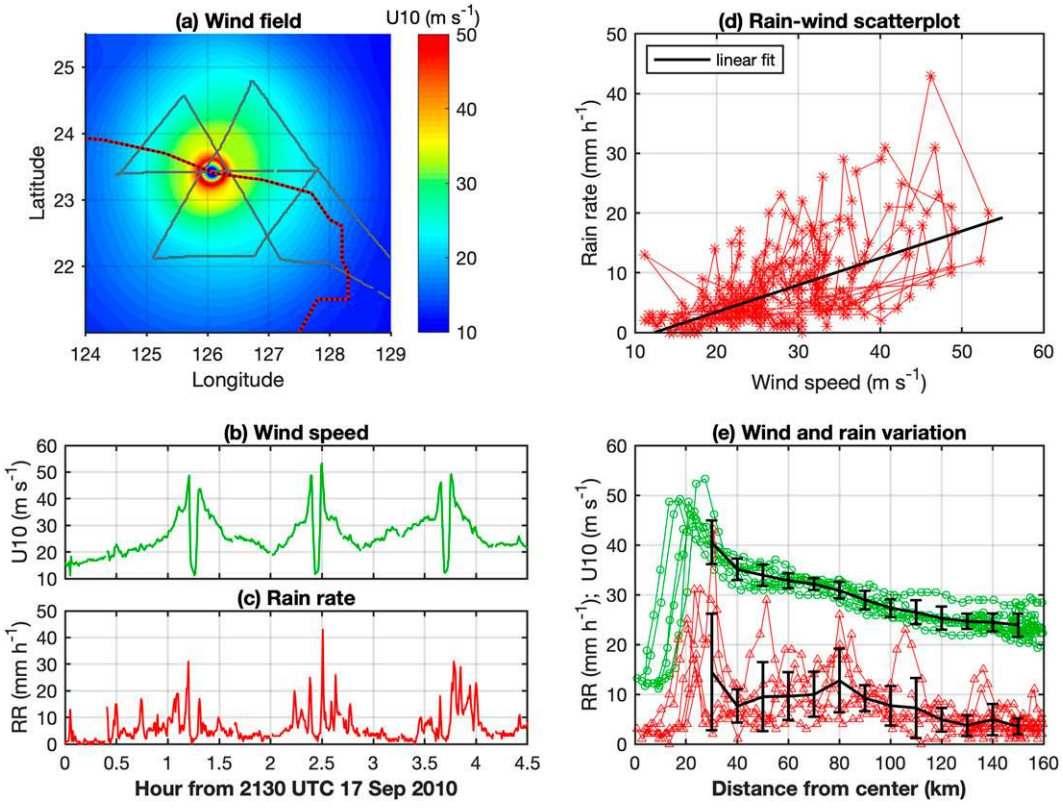

FIG. 3. The surveillance flight in Typhoon Fanapi on 17 Sep 2010: (a) The wind field constructed by simulating the aircraft observations into a parametric wind model. The gray line indicates the flight track. The red line indicates the storm path. (b) Wind speed and (c) rain rate estimated by SFMR on board the aircraft. (d) Rain–wind scatterplot and linear fit, showing that heavy rain is usually associated with high wind. (e) Wind speed and rain rate as a function of distance from the storm center. In 10-km bins, their means and standard deviations are shown as vertical bars.

its low spatial resolution. Fortunately, the PR map shows eyewall and rainbands clearly because of its 250-m spatial resolution. Despite TRMM's wide-swath coverage, there are only a few cases in which our Lagrangian floats and TRMM match both in time and space. Willis (2010) compared the SFMR and TMI estimated rain rates in the western North Pacific (including Fanapi), and found overall good agreements, but with rain rate over 10 mm h^{-1} occurring more frequently in the satellite-based estimates.

3. Rain detection by underwater ambient sound

In this section, we examine underwater ambient sound for signatures of rain. At low winds, the rain-generated sound is much louder than the wind-generated background sound (Fig. 1a), so that rain can be easily detected in underwater ambient sound (Nystuen 2001; Ma et al. 2005). However, the wind-generated background sound increases with increasing wind speed and becomes comparable to sound generated by rain, making it difficult to discriminate them. Here, we demonstrate that rain can be detected by the minute-scale sound fluctuation, instead of absolute sound level used in previous studies.

a. Decomposition of sound measurements

Our decomposition method is illustrated using data segment Q101623 from float 67 (Fig. 5). Figure 5a gives the 30-min sound record measured in Typhoon Megi starting from 2330 UTC 16 October 2010. The broadband sound levels from 40 to 50 kHz have a wide range from 30 to 90 dB. The sound fluctuation at each frequency can be as large as 10 dB. Figure 5e shows wind speed and float depth during this period. The wind speed is about 24 m s^{-1}, higher than the wind condition discussed in Ma et al. (2005). The Lagrangian float ranges from 15 to 42 m in depth as designed. Note that the sound levels are nearly invariable with depth except for a few meters near the surface (refer to Fig. 10 in Zhao et al. 2014). Because of the large variation of background sound with wind speed (Fig. 1), rain cannot be detected using a threshold absolute sound level.

We decompose the underwater ambient sound into three components according to their time scales. First, we calculate background sound, defined as the mean of the lowest 10% sound level over the 30 min period (Fig. 5b). The background sound generally rises and falls with increasing/decreasing wind speed and the presence of bubble clouds (Zhao et al. 2014). Second, sound fluctuation is obtained by removing the background sound from the original data (not shown). Third,

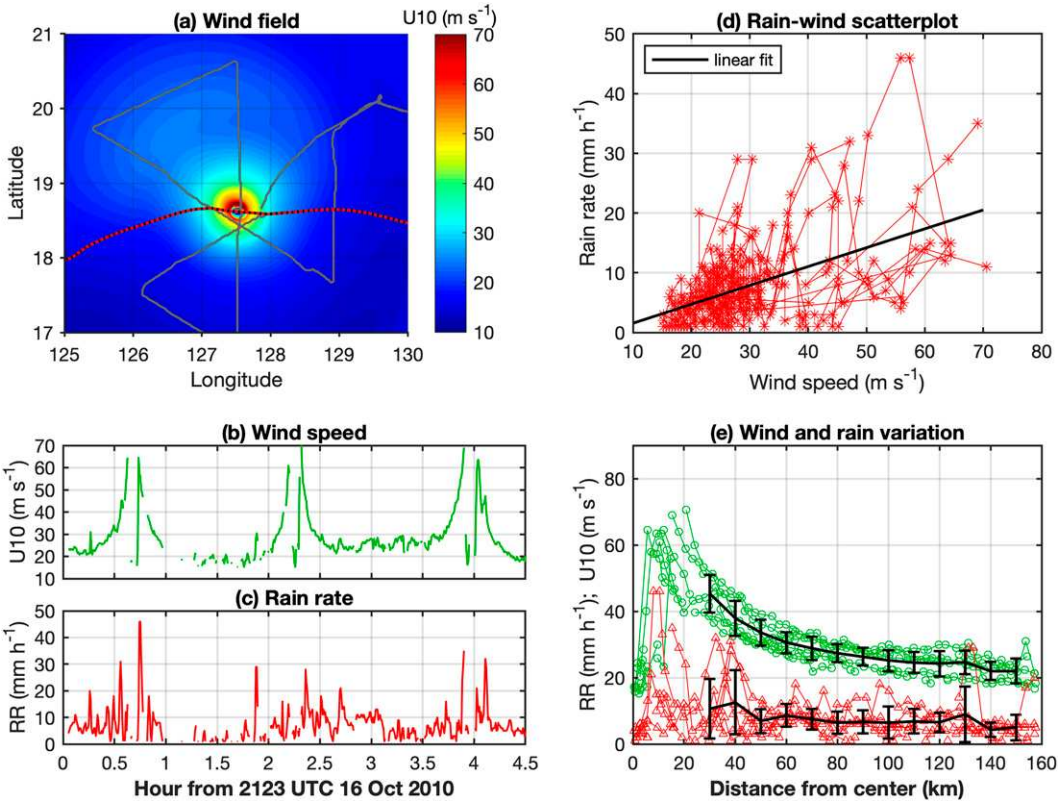

FIG. 4. As in Fig. 3, but for the surveillance flight in Typhoon Megi on 16 Oct 2010.

the sound fluctuation is divided into two components using two matched temporal filters. The second-scale fluctuation is obtained by high-pass filtering the sound fluctuation using 20-s running mean. The minute-scale fluctuation is obtained by low-pass filtering the sound fluctuation. The two components are shown in Figs. 5c and 5d, respectively. By this method, the original underwater ambient sound is decomposed into three components: background, minute-scale fluctuation, and second-scale fluctuation.

Figure 5c reveals that the minute-scale fluctuations may exceed 10 dB and that the loud events may have varying sound spectra. For example, during minutes 10–11, the sound spectra have a peak between 20 and 30 kHz; while during minutes 24–26, the spectra have a peak between 10 and 20 kHz. We argue that these are the acoustic signatures of intermittent rain, and that the spectral variation is due to rain of different rates and different types (Fig. 1). We test this hypothesis below by comparing with TRMM and aircraft observations (section 4). Figure 5d shows the second-scale fluctuation, which contains sound bursts mainly caused by breaking surface waves that usually last for several seconds (Farmer and Vagle 1988). Further analysis will be presented in a separate paper.

Figure 6 shows a high-wind example from float 60 (segment J091801). During this period, the wind speed is 47 m s^{-1} and the float depth ranges from the sea surface to 55 m (Fig. 6e). Figure 6a shows that the sound level is overall very low, in particular, at high frequency, due to the attenuation of bubble clouds in the surface layer (Zhao et al. 2014). In this case, the sound signatures of rain are even harder to detect. Similarly, the minute-scale and second-scale sound fluctuations are given in Figs. 6c and 6d, respectively. When the float is at depth, the high-frequency sound is totally attenuated by bubble clouds. However, there are several loud sound events around the 10 kHz sound, which are interpreted as rain events. We will compare the sound fluctuations with aircraft estimates in section 4b.

b. *Rain detection*

We propose a rain detection method using the minute-scale sound fluctuation (Figs. 5c and 6c). We identify rain by two criteria: 1) the SPL averaged over 5–30 kHz in the minute-scale fluctuation exceeds 4 dB, and 2) the event duration lasts longer than 1 min. In Figs. 5 and 6, the rain events are indicated by a two-level green line. High means rain and low means no rain. This algorithm likely identifies heavy rain events (loud sound), but may miss light rain, and any results derived from it are sensitive to the empirical threshold values (section 5).

We have applied the above decomposition and detection methods to all 408 thirty-minute sound segments from eight Lagrangian floats and created 408 figures with the same format as Figs. 5 and 6. We have archived the denoised sound data, and made them freely available to the community (see data availability statement). Because of the exploratory

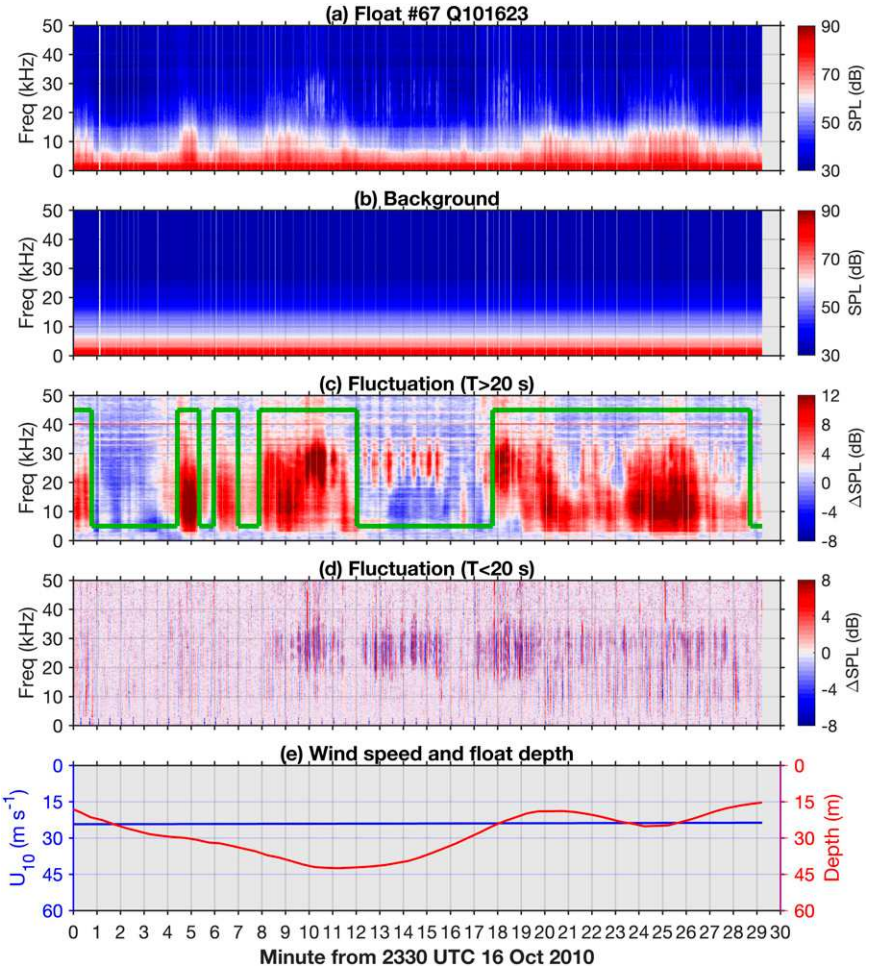

FIG. 5. Decomposition of underwater ambient sound. This example shows one 30-min sound segment from float 67: (a) Underwater ambient sound. (b) Background (30-min mean) sound level. (c) Minute-scale sound fluctuation. (d) Second-scale sound fluctuation. (e) Wind speed and float depth. The sum of (b), (c), and (d) gives (a). The two-level green line in (c) indicates rain (high) or no rain (low).

nature of this work, some parameters are determined empirically. Interested researchers are encouraged to reanalyze the data using their own parameters or methods.

4. Comparisons with aircraft and TRMM observations

In this section, we present four cases of spatially and temporally matched hydrophone and aircraft or satellite observations. We also give a statistical comparison of acoustic and aircraft rain estimates. The consistent features are used to support our method for detecting rain.

a. TRMM and aircraft observations in Typhoon Megi

Our first case compares the hydrophone measurements with TRMM and aircraft observations in Typhoon Megi on 16 October 2010 (Fig. 7). Figures 7a and 7b present the rain maps observed by the TMI and the PR at 2337 UTC 16 October 2010. Figure 7a shows a large map of precipitation associated with Megi, due to the TMI's 878-km wide swath. However, its 5-km spatial resolution is insufficient to resolve small-scale rain structures. Thanks to the PR's 247-km swath and 0.25–0.3-km spatial resolution, Fig. 7b shows a small rain map with higher spatial resolution. One can see the rainband at the eyewall and several outer rainbands. At the imaging time, the WC-130J aircraft was within the storm center (Figs. 7a,b, green dots) and flew northward (blue line). Figure 7c plots the rain rates along the section estimated by the SFMR, the PR and the TMI. During this period, float 67 was to the north of the storm (Figs. 7a,b, black circles) and its horizontal drift was negligible. Figure 7d gives the minute-scale sound fluctuation observed by float 67 and rain events detected in the sound fluctuation (Fig. 5c). Floats 66 and 68 were nearby but in sleep mode (not shown).

We found two consistent features between the hydrophone and TRMM observations. First, both suggest rain during minutes 5–12. Float 67 shows loud events in sound fluctuation, which are attributed to rain (green line) and the nearly

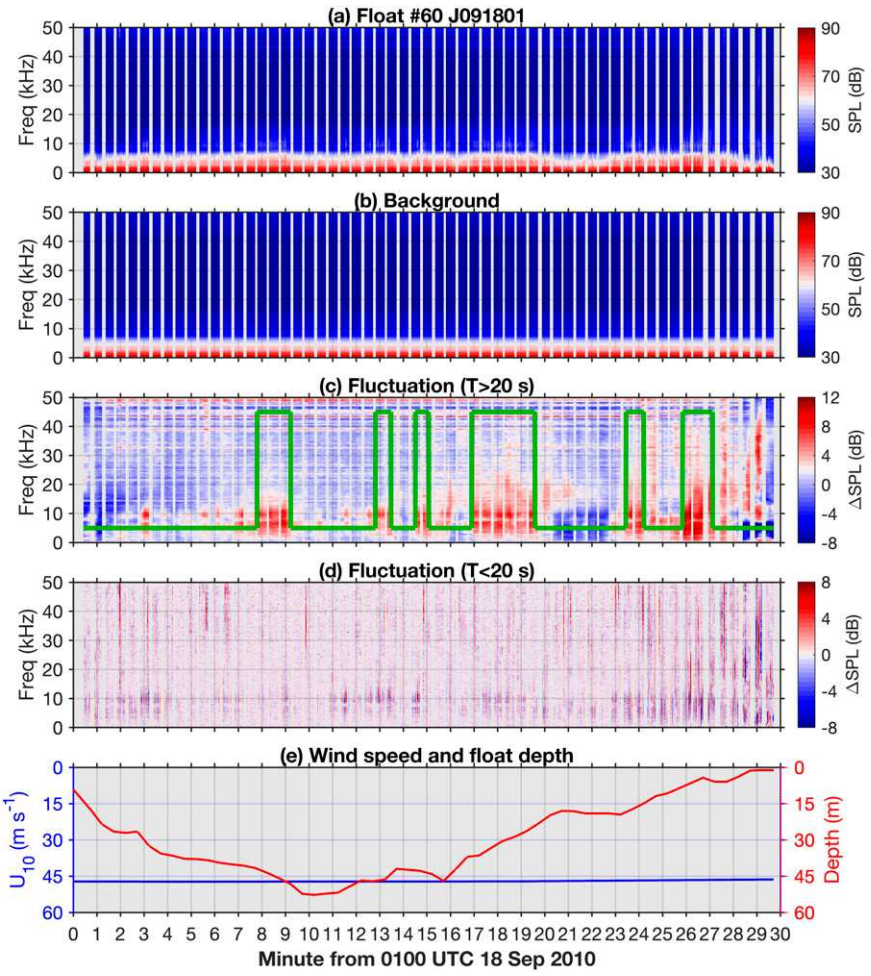

FIG. 6. As in Fig. 5, but for one 30-min sound segment from float 60. The wind speed during this period is about 47 m s^{-1}.

simultaneous TRMM image shows float 67 in a rainband (Figs. 7a,b). These observations are matched both in time and space. Second, both indicate intermittent rain during the 30-min period. The hydrophone minute-scale fluctuation suggests several rain events. Meanwhile, the TMI and PR rain maps show that float 67 was surrounded by rainbands. Thus, TRMM and hydrophone both show intermittent rain events and varying rain rate during this period. Although it is hard to compare them point by point, the data are consistent with our hypothesis that the minute-scale sound fluctuation is caused by rain.

Figure 7c compares the rain rates from three instruments: the PR, the TMI, and the SFMR. They all yield rain rates of 25–35 mm h^{-1} at the eyewall around minute 15. Before minute 15, however, the TMI estimates are much larger, which may be caused by the different spatial resolutions between TMI and SFMR. This discrepancy explains the difficulty in comparing rain rates from different techniques, even though they match in space and time.

b. *Aircraft observations in Typhoon Fanapi*

Our second case compares the hydrophone measurements with aircraft observations in Typhoon Fanapi on 17 September 2010 (Fig. 8). Figure 8a shows the flight track overlying the wind field. The WC-130J aircraft flew within 14 km of float 60 at minute 7 and within 1 km of float 62 at minute 25 (float 61 was in sleep mode). The aircraft was in the storm center during minutes 9–14. Figure 8b plots wind speed and rain rate along the leg (Fig. 8a, magenta section). The wind speed is low around minutes 9–14, because the aircraft was inside the eye. Float 60 was at the eyewall with a wind speed of 47 m s^{-1}. Float 62 was about 100 km from the center with a wind speed of 30 m s^{-1}. Sound measurements from both floats suggest several rain events in this period. The sound fluctuation from float 60 suggests a rain event during minutes 7–8 (Fig. 8c), consistent with the aircraft estimated rain rate (Fig. 8b). The sound fluctuation from float 62 suggests a rain event during minutes 25–26 (Fig. 8d), consistent with the aircraft estimated rain rate (Fig. 8b). These consistent observations support our hypothesis that the minute-scale sound fluctuation is caused by rain.

c. *TRMM observations in Typhoon Fanapi*

Our third case compares the TRMM rain estimates and hydrophone sound measurements in Typhoon Fanapi on

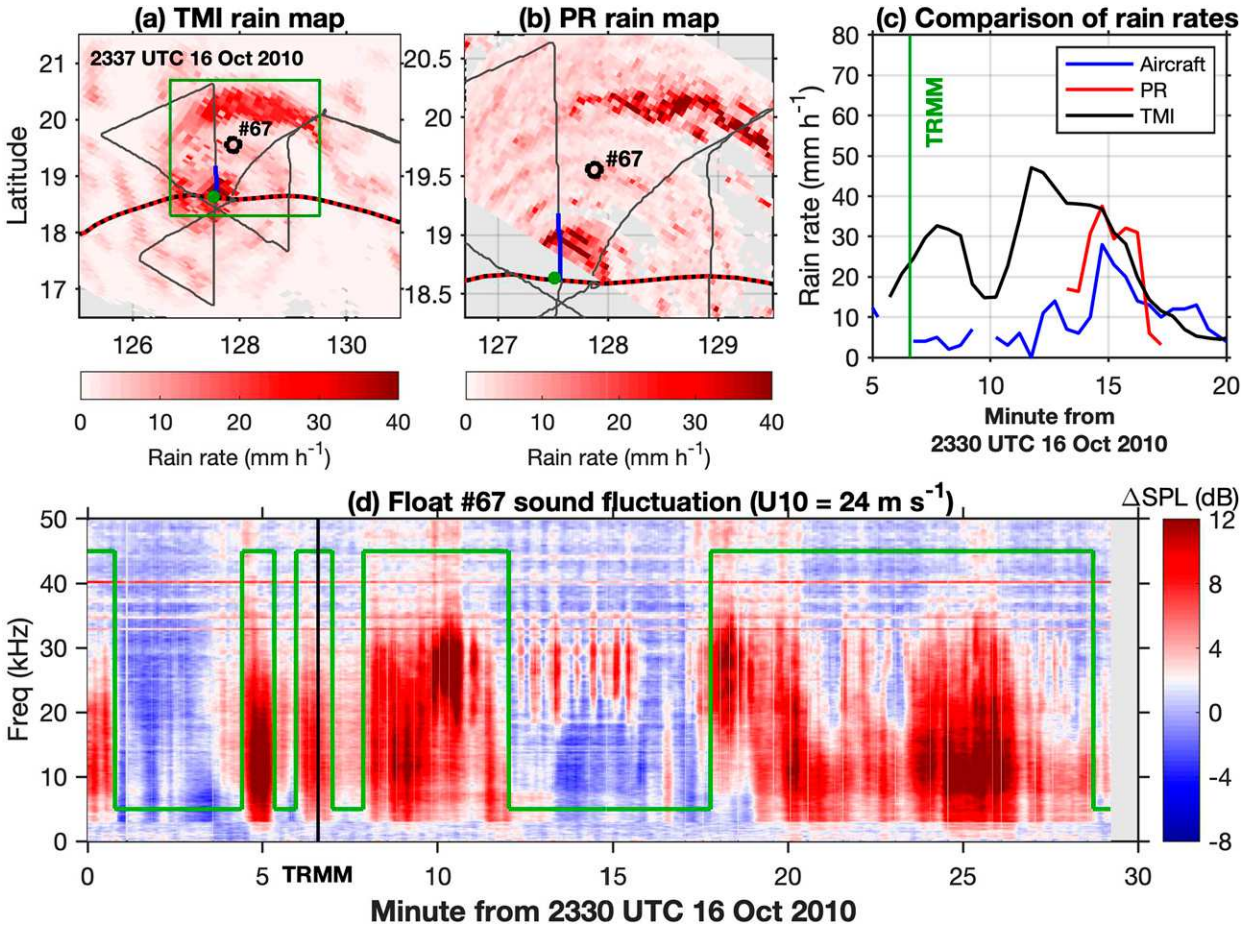

FIG. 7. Comparison of rain observations by TRMM, aircraft, and hydrophone: (a) TMI rain map. (b) PR rain map. The spatial coverage of (b) is shown by a green-outlined box in (a). The TRMM observation time is 2337 UTC 16 Oct 2010. Dotted lines indicate the track of Typhoon Fanapi. Gray lines indicate the flight track. The black circle denotes the current location of float 67. The green dot denotes the current location of the aircraft, which was flying from south to north along one leg. (c) Rain rates estimated by TMI, PR, and SFMR in 15 min along the blue section in (b). (d) Minute-scale sound fluctuation from float 67 (Fig. 5c). The TRMM observation time is labeled by the vertical line. The two-level green line indicates rain (high) or no rain (low).

18 September 2010 (Fig. 9). The TMI and PR rain maps are shown in Figs. 9a and 9b, respectively. The TMI map fully covers the storm with a low spatial resolution. The PR map has a high spatial resolution, but only covers the northern part of the storm. The locations of floats 60 and 62 are indicated by two circles (float 61 was in sleep mode). Figures 9c and 9d give the minute-scale sound fluctuations measured by these two floats. The wind speed for both floats was 17–18 m s^{-1}. One can see that floats 60 and 62 have different rain conditions. Float 62 detects several rain events, consistent with the TMI rain map (Fig. 9a) that shows it was on the rainy side of Fanapi. This qualitative consistency supports our hypothesis that the minute-scale sound fluctuation is caused by rain.

However, float 60 detects no rain events in the 30-min period and, in particular, at the time that the TRMM satellite flew over the site (minute 25). The weak fluctuations in sound at 30–50 kHz may be due to light rain at low wind speeds (Fig. 1a, III), but were missed by our detection algorithm. The TMI rain map (Fig. 9a) shows float 62 was on the dry side of Fanapi. The PR map shows that float 60 was on the edge of a rain event. It was thus ambiguous as to whether it was raining. Considering the intermittent and complex nature of rain, these observations are generally consistent with our hypothesis that the minute-scale sound fluctuation is caused by rain.

d. Radar observations in Hurricane Gustav

Our final case compares the matched hydrophone measurements with the lower-fuselage radar images from the NOAA WP-3D aircraft in Hurricane Gustav. Because of the wide swath of the radar images (with a radius of about 200 km), comparisons can be made over a period of 10 min, as the aircraft was about 170 km northwest of the float. The sound fluctuation from float 50 suggests one rain event lasting about 6 min (Fig. 10a). The rain event was captured by the radar images, which show one rain cloud (high reflectivity) moving across float 50 from south to north (Figs. 10b–i). At

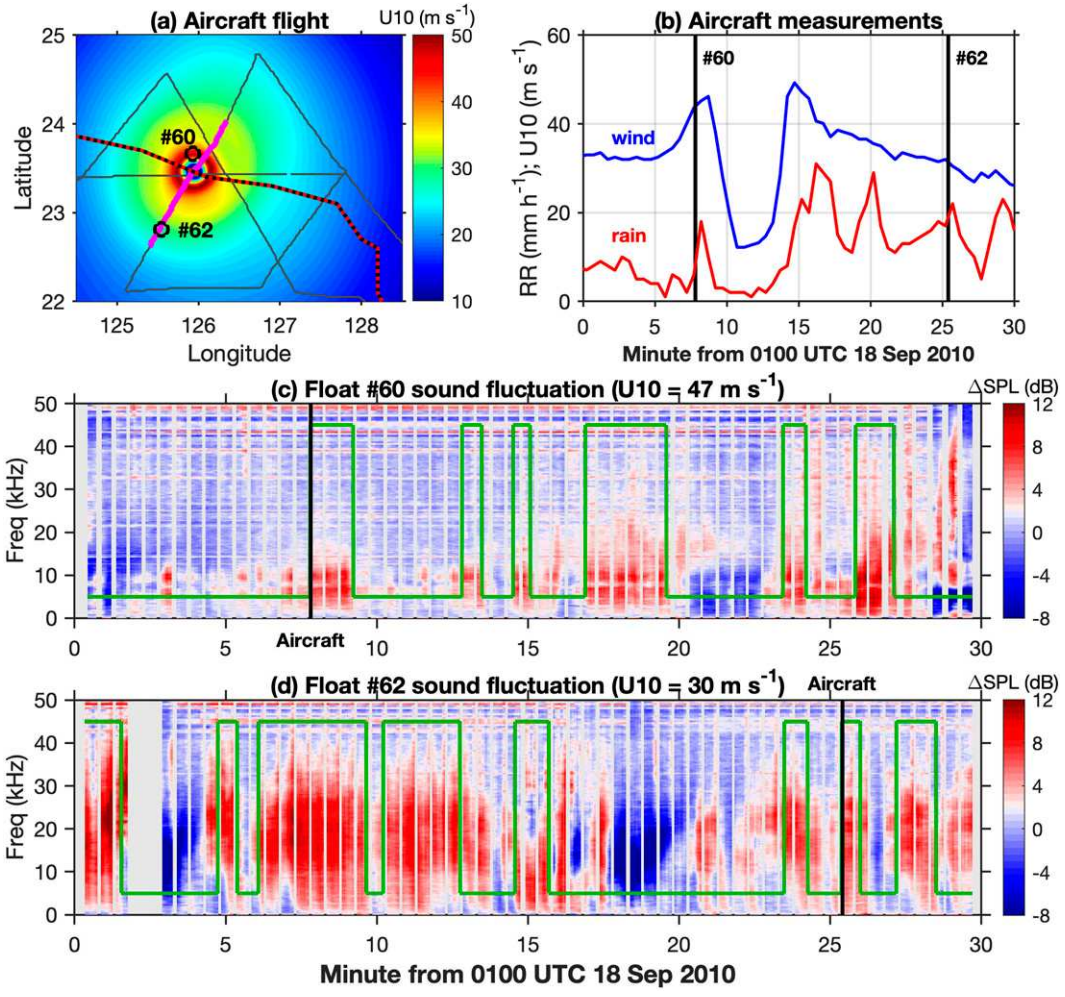

FIG. 8. Comparison of the rain observations by SFMR (aboard aircraft) and hydrophone in Typhoon Fanapi: (a) Wind field superimposed with the storm path (dashed line), flight track (gray line), and float positions (circles). (b) SFMR estimated wind speed and rain rate along the magenta section in (a). (c) Minute-scale sound fluctuation from float 60. (d) Minute-scale sound fluctuation from float 62. Float 61 was in sleep mode. The vertical lines label the times the aircraft flew over the floats. The two-level green lines indicate rain (high) or no rain (low).

minutes 7–8 (Fig. 10b), float 50 was at the northern edge of the rain cloud; rain was not detected at the float (Fig. 10a). The following six images over 9 min show that the float was beneath the rain cloud and that rain was detected by the float. By minute 17, the rain cloud moved past the float (Fig. 10i); thus, no rain was detected at the float again (Fig. 10a). This excellent correspondence between the hydrophone measurements and aircraft observations strongly supports our hypothesis that the minute-scale sound fluctuation is caused by rain.

e. Variability in wind, rain, and sound

We hypothesize that the minute-scale sound fluctuations are mainly due to rain. An alternative hypothesis is that they are due to minute-scale wind variations. Here we examine the two possibilities by comparing their contributions to sound fluctuations. We first examine the variation coefficient Cv using aircraft SFMR-estimated wind and rain. As described in section 2b, both of the wind and rain estimates are 30-s averaged; therefore, they can resolve minute-scale fluctuations but miss the <30-s high-frequency variation. Here Cv is defined to be the ratio of the standard deviation to the mean, which are from the 10-km binned values shown in Figs. 3e and 4e. Figure 11a shows that Cv is 4%–17% for wind and 28%–110% for rain, indicating that rain is much more variable than wind. Furthermore, Fig. 11b presents the standard deviation of minute-scale sound fluctuations at 8 kHz for each 30-min segment (section 2a). It shows that the typical values for winds > 20 m s^{-1} are 4 ± 2 dB. Segments with rain generally have larger fluctuations than those without rain. This feature is also consistent with the idea that the minute-scale sound fluctuations are mainly due to rain. But the argument is circular and not definitive, because the rain classification (larger fluctuation) implies this result (section 3b).

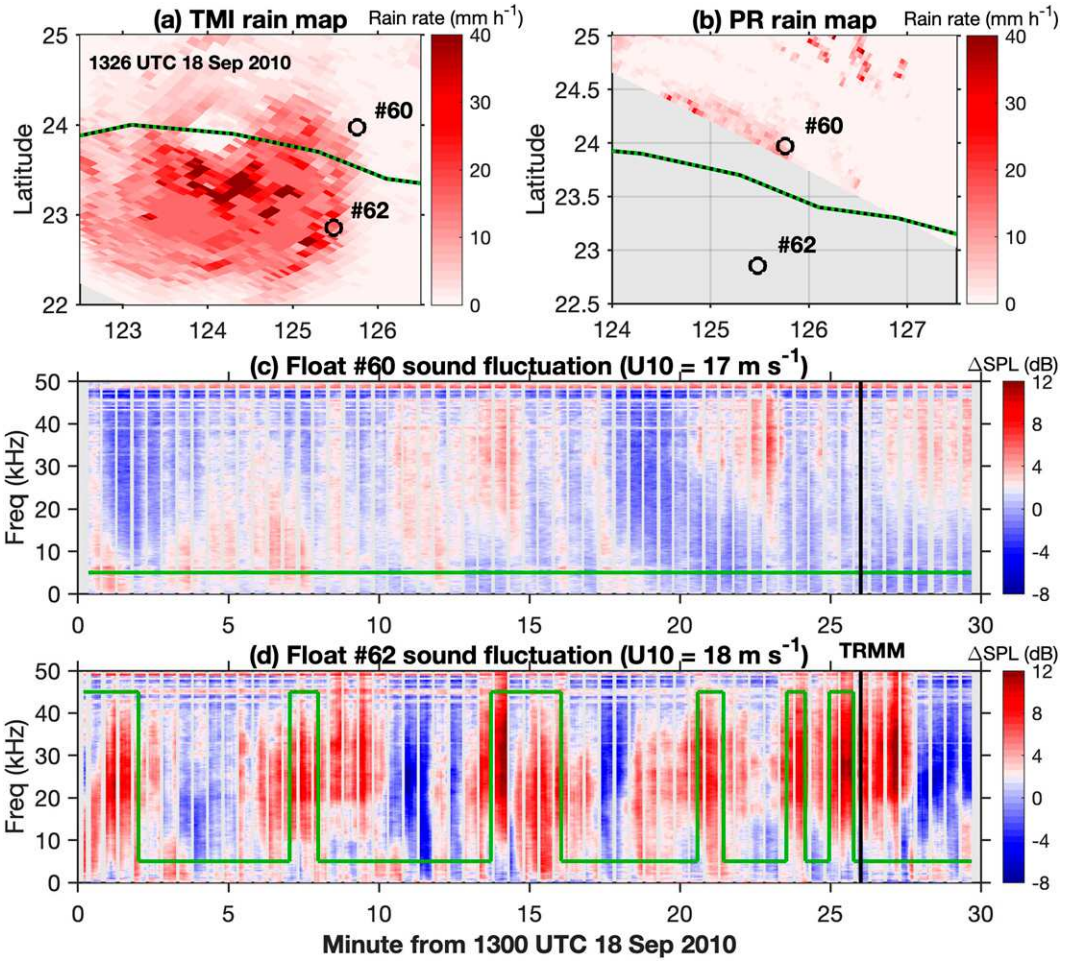

FIG. 9. Comparison of rain observations by TRMM and hydrophone in Typhoon Fanapi: (a) TMI rain map. (b) PR rain map. The TRMM observation time is 1326 UTC 18 Sep 2010. Dashed lines indicate the track of Fanapi. Black circles indicate the present locations of floats 60 and 62. (c) Minute-scale sound fluctuation observed by float 60. (d) Minute-scale sound fluctuation observed by float 62. The TRMM observation time is labeled by vertical lines. The two-level green lines indicate rain (high) or no rain (low).

Could the sound fluctuations be due to wind fluctuations? The black line in Fig. 12a shows the 5-kHz sound level as a function of wind speed from Fig. 11 in Zhao et al. (2014). The colored dots show the variation of sound level due to wind fluctuations assuming Cv = 8% (refer to Fig. 11a, green lines) for winds of 20, 30, and 40 m s^{-1}. This is simulated by randomly varying the wind speed with Gaussian noise specified by Cv for each wind speed category in 3000 realizations. The resulting standard deviation in sound level indicates that fluctuations of less than 2 dB result from winds of 20 and 30 m s^{-1} (Fig. 12b, red and blue bars).

Could the sound fluctuations be due to rain fluctuations? The black line in Fig. 12c shows the 8-kHz sound level as a function of wind speed from Eq. (2). The colored dots show the variation of sound level due to rain fluctuations assuming Cv = 60% (refer to Fig. 11a, red lines) for rain rates of 0.1, 1, and 10 mm h^{-1}. This is simulated by randomly varying the rain rate with Gaussian noise specified by Cv for each category for 3000 realizations. Figure 12d gives the resulting standard deviation of sound level. It shows that the rain-induced sound fluctuations are about 6 dB larger independent of rain rate (blue and red bars).

In summary, for winds < 35 m s^{-1}, the wind variations are too small to explain the observed minute-scale sound fluctuations at 8 kHz. At all rain rates, the rain fluctuations slightly overestimate the observed 8-kHz sound fluctuation, perhaps because the model is for 5 kHz rather than 8 kHz or because the model does not work well at these high wind speeds. Nevertheless, this supports the idea that the minute-scale sound fluctuations are mainly due to rain. For winds > 40 m s^{-1}, however, the sound level at 8 kHz decreases dramatically because of increasing bubble absorption, and the sound fluctuations due to wind fluctuations are of the same magnitude as those of rain. Thus, rain and wind may both contribute to minute-scale sound

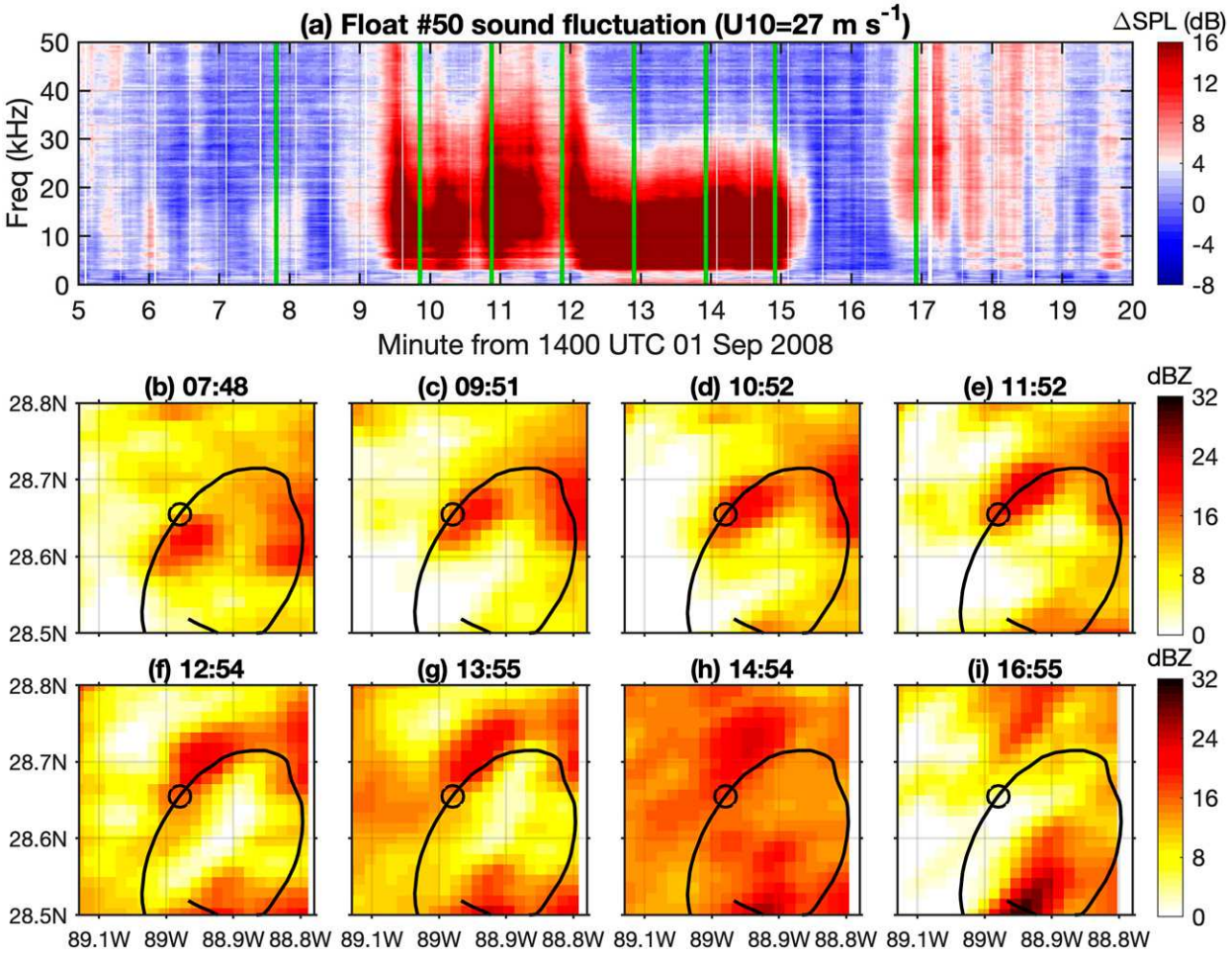

FIG. 10. Comparison of sound fluctuation and radar reflectivity: (a) Minute-scale sound fluctuation from float 50 in Gustav. Rain is detected during minutes 9–16. (b)–(i) Reflectivity images from lower-fuselage radar aboard the NOAA WP-3D aircraft. Their imaging times are labeled in (a) by vertical lines. The black curves and circles indicate the trajectory of float 50 and its present location. Sound fluctuation and high-reflectivity cloud correspond well in time and space.

fluctuations, which makes it even more challenging to detect rain, if possible.

5. Rain features in tropical cyclones

a. Sound spectra of rain

In this section, we examine the sound spectra of rain by comparing spectra from sound segments in which rain is detected and not detected (section 3b). The sound measurements with rain are further divided into six groups by wind speed, from which six sound spectra are obtained. The resultant sound spectra with rain are shown in Fig. 13a. Similarly, six sound spectra without rain are calculated and shown in Fig. 13b. The sound spectra with and without rain both decrease with increasing wind speed, because of the attenuation by bubble clouds.

Figure 13c gives the spectral differences between Figs. 13a and 13b. It shows that the sound signature of rain is strongest between 5 and 10 kHz and has a maximum amplitude of about 8 dB. In tropical cyclones, convective rains have large raindrops that produce loud sound across a wide frequency range as shown in Fig. 1 (Nystuen et al. 1993; Ma et al. 2005). The spectra in Fig. 13c are more strongly peaked. This may be due to three factors: 1) at low frequencies and high winds, the wind noise is louder than the rain noise, so the rain noise cannot be detected; 2) at high frequencies and high winds, bubble clouds attenuate sound, including the rain noise; 3) our rain detection method uses the amplitude at 5–30 kHz, which may bias the rain spectra toward a peak at those frequencies.

b. Statistics of rain events

Here we examine rain events and rain time derived from underwater ambient sound. According to our method and criteria, we have detected a large number of rain events with varying duration times. For example, there are five rain events in segment Q101623 (Fig. 5) and six rain events in segment J091801 (Fig. 6). A total of 723 rain events have been identified in all the sound measurements by the eight

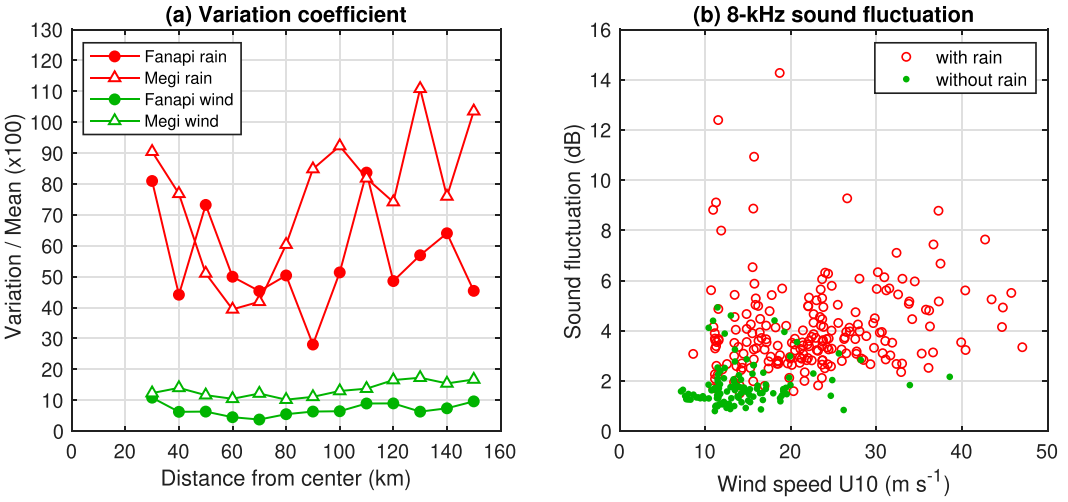

FIG. 11. (a) Variation coefficient defined as the ratio of the standard deviation to the mean (Fig. 3e for Fanapi and Fig. 4e for Megi). Rain (red) is more intermittent than wind (green). (b) The 8-kHz sound fluctuation from all eight floats. Each symbol represents one 30-min sound segment. Red circles and green dots indicate sound segments with and without rain, respectively.

floats. The statistics of the rain events are given in Fig. 14. Figure 14a shows that the rain events usually last for a few minutes, rarely longer than 10 min. This feature is consistent with the fast translation speed and the spatial rainband pattern of tropical cyclones. Figure 14b shows the rain time in percentage for all floats. Rain time accounts for 8%–16% of the total observation time. There are no notable differences among the three tropical cyclones (Gustav, Fanapi, and Megi). Again, the statistical results are sensitive to our empirical threshold values. Some light rain may be missed in our statistics (Fig. 9c). Future comprehensive algorithms are needed to address the complex nature of rain in tropical cyclones.

c. *Estimation of rain rate*

Ma et al. (2005) developed an empirical relation between sound level and rain rate using 90 months of simultaneous underwater sound measurements and traditional rain gauge measurements (Fig. 15a). They found that rain has signatures in the 1–10-kHz-frequency bands and built an empirical algorithm for estimating rain rate using 5-kHz sound, that is, Eq. (2).

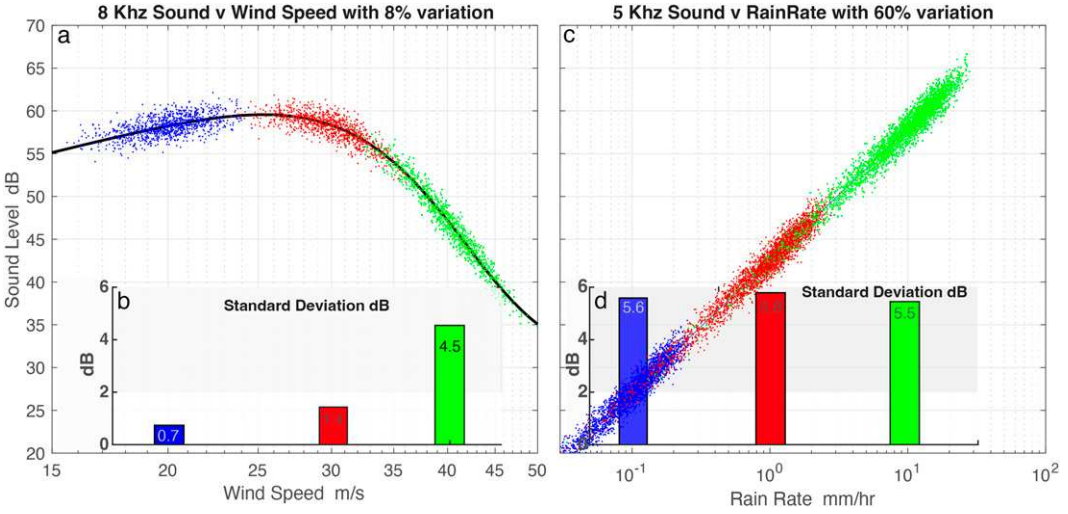

FIG. 12. (a) The 8-kHz sound fluctuation due to rain variation. The black line shows the relation between sound level and wind speed from Fig. 11 in Zhao et al. (2014). The dots show the sound level due to wind variation around three wind speeds. (b) The standard deviation (colored bars) of the colored dots in (a). (c) As in (a), but for the 5-kHz sound fluctuation due to rain variation. The black line shows the relation between sound level and rain rate in Ma et al. (2005). (d) The standard deviation (colored bars) of the colored dots in (c). The sound fluctuations induced by rain variation are much greater than those induced by wind variation.

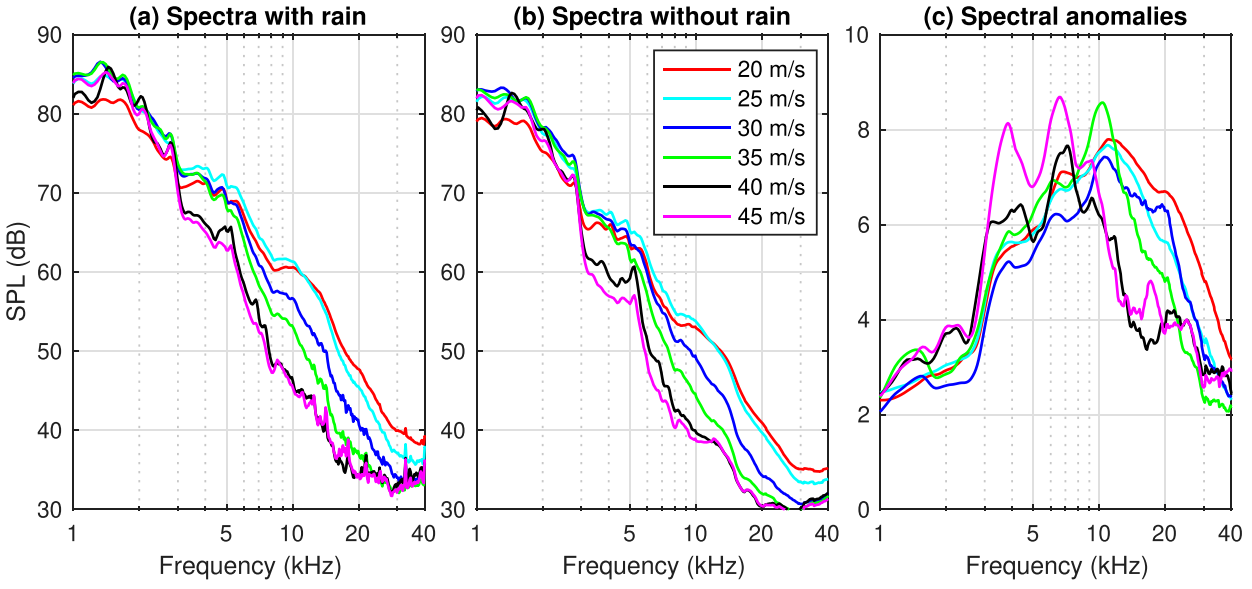

FIG. 13. Spectra of underwater ambient sound with and without rain: (a) Spectra with rain. (b) Spectra without rain. (c) Differences between (a) and (b). The spectral anomalies caused by rain are 2–8 dB, with a peak around 10 kHz. The rain signatures in >10-kHz sound weaken with increasing wind partly because of bubble clouds.

However, we cannot directly extend this low-wind algorithm to the high-wind regime. To illustrate the challenge, the 5-, 10-, and 20-kHz sound levels are given in Fig. 15b. They all first increase and then decrease with increasing wind speed, due to breaking wind waves and bubble clouds. Such a feature has been shown in contrasting the 5- and 20-kHz sound levels (Nystuen 2001; Zhao et al. 2014). The sound levels are not a monotonic function of wind speed; therefore, it is challenging to develop an algorithm for estimating rain rate in tropical cyclones. Fortunately, the sound levels of different frequencies have different response functions (Fig. 15b, black lines), suggesting that a multifrequency algorithm is feasible.

It is premature to develop such an algorithm in this paper because of the lack of simultaneous measurements. For the low-wind condition, Ma et al. (2005) collected 90 months of simultaneous measurements. Here, we have only a limited number of cases where sound measurements match aircraft or TRMM estimates. Note that traditional rain gauges do not function well in the harsh tropical cyclones. Even worse, the aircraft and TRMM rain estimates have large uncertainties in rain rate, as evidenced by the notable discrepancies among them (e.g., Fig. 7c). All of these features suggest the challenge as well as the importance of developing the underwater ambient sound technique for studying rain in tropical cyclones.

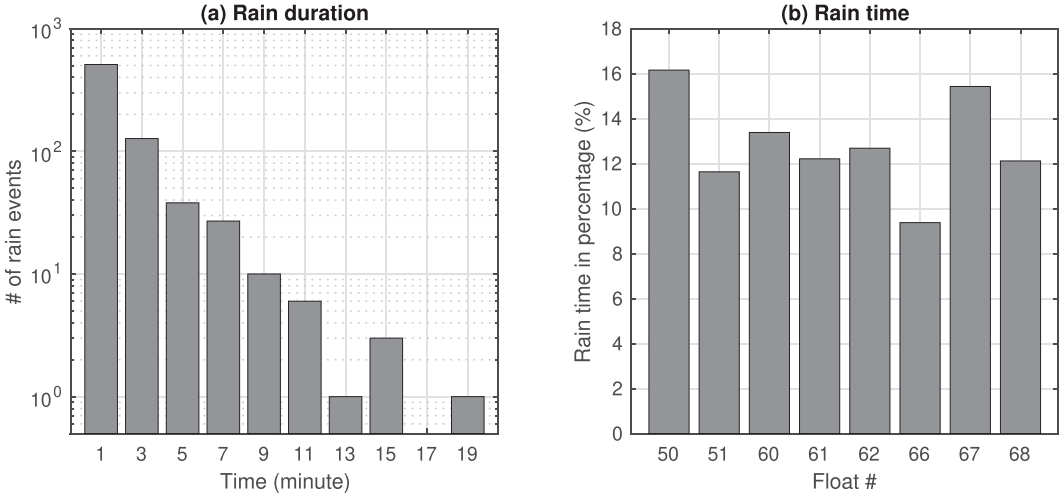

FIG. 14. Statistics of rain events in tropical cyclones: (a) Histogram of rain duration. (b) Histogram of rain time (%). The statistics are sensitive to the empirical threshold values in the detection method.

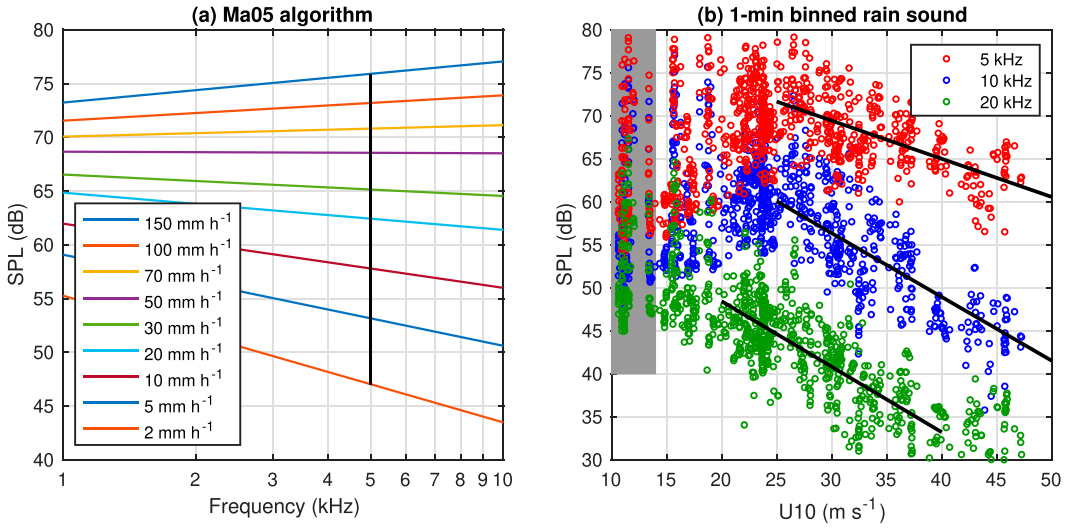

FIG. 15. Estimation of rain rate using underwater ambient sound: (a) The Ma05 algorithm developed in the low-wind condition. The lines are plotted using Eqs. (6)–(8) in Ma et al. (2005). (b) The 5-, 10-, and 20-kHz sound levels (with rain). The Ma05 algorithm is applicable to the low-wind condition (gray box). At winds > 15 m s^{-1}, the sound level is significantly affected by wind speed. Different sound frequencies have different response curves (black lines), suggesting that high-wind algorithms can be developed using multifrequency sound.

6. Summary

Rain plays an important role at the air–sea interface in tropical cyclones and is a major destructive factor of these storms. Previous rain estimates by aircraft and satellites have limited spatiotemporal coverage and large uncertainties; thus, any new technique to estimate rain rate is valuable. Ma et al. (2005) developed an algorithm for estimating rain rate using underwater ambient sound for the low-wind regime, but it cannot be extended to the high-wind regime of tropical cyclones. At high winds, the wind- and rain-generated sound levels are comparable, and both are attenuated by bubble clouds in the surface layer. These processes lead to a complex variation of sound with wind and rain; therefore, rain cannot be detected from absolute sound level.

We explored the possibility of measuring rain by underwater ambient sound using rare sound measurements made by hydrophones on board Lagrangian floats in tropical cyclones. We searched aircraft and satellite observations in these field experiments and found a few spatially and temporally matched cases among these observations. To detect the sound signatures of rain, we proposed a method to decompose ambient sound into three components (Figs. 5 and 6): (i) background, that is the 30-min mean for each sound segment, (ii) second-scale fluctuation, that is for periods shorter than 20 s, and (iii) minute-scale fluctuation between 30 min and 20 s. Among them, the second-scale fast fluctuations are primarily due to surface wave breaking and the >30-min slow fluctuations are due to rising/falling wind and bubble clouds with the passage of tropical cyclones (Zhao et al. 2014).

We argue that the minute-scale sound fluctuations are primarily the sound signatures of rain. In the minute-scale sound fluctuation, we detect rain using the following two criteria: (i) the sound level averaged over 5–30 kHz is greater than 4 dB, and (ii) the event duration is longer than 1 min (Figs. 5 and 6). Our detection method was supported by the following consistent features:

- A spatial and temporal match between acoustic rain detection and satellite and/or aircraft estimates was found in three cases. The acoustic rain detection is consistent with the satellite or aircraft rain estimates (Figs. 7–9).
- An outstanding 6-min-long rain event in Hurricane Gustav was consistently detected by both underwater ambient sound and the active lower-fuselage radar aboard the NOAA WP-3D aircraft (Fig. 10).
- For wind speeds < 40 m s^{-1}, the minute-scale sound fluctuations are much larger than would be expected from wind variations and are comparable to those expected for rain variations, supporting the attribution of the minute-scale fluctuations to rain (Figs. 11 and 12). However, our data are barely sufficient to justify the detection method, and surely insufficient to produce a useful algorithm for estimating rain rate from ambient sound.

We examined the features of rain in tropical cyclones using the rain events derived from underwater ambient sound. It was found that rain makes sound of 2–8 dB louder in a wide band from 1 to 40 kHz, consistent with large raindrops of convective rain typical of tropical cyclones. The peak sound level appears around 5–10 kHz (Fig. 13). A total of 723 rain events were detected in 190 h of data, accounting for 8%–16% of the time. Each rain event lasts for a few minutes and rarely longer than 10 min (Fig. 14). Note that our results are sensitive to the empirical threshold values (4 dB and 1 min) in the rain detection method. To avoid misinterpretation, we make our sound data freely available to the community (see data availability statement).

The algorithm for estimating rain rate from underwater ambient sound in the low-wind condition (Ma et al. 2005) cannot be extended to the high-wind regime of tropical cyclones. We observed that the sound levels at different frequencies have different response curves (Fig. 15), which suggests that future empirical algorithms can be developed using multifrequency ambient sound. The development of such algorithms requires simultaneous and collocated measurements of rain rate and ambient sound spanning at least the 5–20-kHz-frequency range, at a sampling rate of 1 Hz or higher, and continuously in several tropical cyclones.

Acknowledgments. This work was supported by University of Washington Royalty Research Fund A97863 and NSF Project OCE1756412. We thank Peter Blake, Barry Ma, and Shuyi Chen for their helpful suggestions. We thank two anonymous reviewers for their constructive suggestions that have greatly improved this paper. This work is dedicated to the memory of Jeffery Nystuen for his pioneering work on measuring wind and rain by underwater ambient sound.

Data availability statement. The TRMM TCFP data are from the NASA EOSDIS Global Hydrology Resource Center in Huntsville, Alabama (https://doi.org/10.5067/TRMM/TCPF-L1/DATA201). The SFMR data (https://www.aoml.noaa.gov/hrd/Storm_pages/gustav2008) and lower-fuselage radar images (https://www.aoml.noaa.gov/hrd/Storm_pages/gustav2008/radar.html) are from the Hurricane Research Division of the Atlantic Oceanographic and Meteorological Laboratory of the National Oceanic and Atmospheric Administration. The underwater ambient sound data are freely available to the public (https://doi.org/10.5281/zenodo.8151199).

REFERENCES

D'Asaro, E., and Coauthors, 2011: Typhoon-ocean interaction in the western North Pacific: Part 1. *Oceanography*, **24** (4), 24–31, https://doi.org/10.5670/oceanog.2011.91.

——, and Coauthors, 2014: Impact of typhoons on the ocean in the Pacific: ITOP. *Bull. Amer. Meteor. Soc.*, **95**, 1405–1418, https://doi.org/10.1175/BAMS-D-12-00104.1.

Emanuel, K., 2017: Assessing the present and future probability of Hurricane Harvey's rainfall. *Proc. Natl. Acad. Sci.*, **114**, 12 681–12 684, https://doi.org/10.1073/pnas.1716222114.

Farmer, D. M., and D. D. Lemon, 1984: The influence of bubbles on ambient noise in the ocean at high wind speeds. *J. Phys. Oceanogr.*, **14**, 1762–1778, https://doi.org/10.1175/1520-0485(1984)014<1762:TIOBOA>2.0.CO;2.

——, and S. Vagle, 1988: On the determination of breaking surface wave distributions using ambient sound. *J. Geophys. Res.*, **93**, 3591–3600, https://doi.org/10.1029/JC093iC04p03591.

Hou, A. Y., and Coauthors, 2014: The Global Precipitation Measurement mission. *Bull. Amer. Meteor. Soc.*, **95**, 701–722, https://doi.org/10.1175/BAMS-D-13-00164.1.

Houze, R. A., Jr., and Coauthors, 2006: The Hurricane Rainband and Intensity Change Experiment: Observations and modeling of Hurricanes Katrina, Ophelia, and Rita. *Bull. Amer. Meteor. Soc.*, **87**, 1503–1522, https://doi.org/10.1175/BAMS-87-11-1503.

Hsu, J.-Y., R.-C. Lien, E. A. D'Asaro, and T. B. Sanford, 2017: Estimates of surface wind stress and drag coefficients in Typhoon Megi. *J. Phys. Oceanogr.*, **47**, 545–565, https://doi.org/10.1175/JPO-D-16-0069.1.

——, ——, ——, and ——, 2019: Scaling of drag coefficients under five tropical cyclones. *Geophys. Res. Lett.*, **46**, 3349–3358, https://doi.org/10.1029/2018GL081574.

Jiang, H., P. G. Black, E. J. Zipser, F. D. Marks, and E. W. Uhlhorn, 2006: Validation of rain-rate estimation in hurricanes from the Stepped Frequency Microwave Radiometer: Algorithm correction and error analysis. *J. Atmos. Sci.*, **63**, 252–267, https://doi.org/10.1175/JAS3605.1.

——, C. Liu, and E. J. Zipser, 2011: A TRMM-based tropical cyclone cloud and precipitation feature database. *J. Appl. Meteor. Climatol.*, **50**, 1255–1274, https://doi.org/10.1175/2011JAMC2662.1.

Klotz, B. W., and E. W. Uhlhorn, 2014: Improved Stepped Frequency Microwave Radiometer tropical cyclone surface winds in heavy precipitation. *J. Atmos. Oceanic Technol.*, **31**, 2392–2408, https://doi.org/10.1175/JTECH-D-14-00028.1.

Kummerow, C., W. Barnes, T. Kozu, J. Shiue, and J. Simpson, 1998: The Tropical Rainfall Measuring Mission (TRMM) sensor package. *J. Atmos. Oceanic Technol.*, **15**, 809–817, https://doi.org/10.1175/1520-0426(1998)015<0809:TTRMMT>2.0.CO;2.

Lin, I.-I., and Coauthors, 2013: An ocean coupling potential intensity index for tropical cyclones. *Geophys. Res. Lett.*, **40**, 1878–1882, https://doi.org/10.1002/grl.50091.

Ma, B. B., J. A. Nystuen, and R.-C. Lien, 2005: Prediction of underwater sound levels from rain and wind. *J. Acoust. Soc. Amer.*, **117**, 3555–3565, https://doi.org/10.1121/1.1910283.

Medwin, H., J. A. Nystuen, P. W. Jacobus, L. H. Ostwald, and D. E. Snyder, 1992: The anatomy of underwater rain noise. *J. Acoust. Soc. Amer.*, **92**, 1613–1623, https://doi.org/10.1121/1.403902.

Mrvaljevic, R. K., and Coauthors, 2013: Observations of the cold wake of Typhoon Fanapi (2010). *Geophys. Res. Lett.*, **40**, 316–321, https://doi.org/10.1029/2012GL054282.

Nystuen, J. A., 1996: Acoustical rainfall analysis: Rainfall drop size distribution using the underwater sound field. *J. Atmos. Oceanic Technol.*, **13**, 74–84, https://doi.org/10.1175/1520-0426(1996)013<0074:ARARDS>2.0.CO;2.

——, 2001: Listening to raindrops from underwater: An acoustic disdrometer. *J. Atmos. Oceanic Technol.*, **18**, 1640–1657, https://doi.org/10.1175/1520-0426(2001)018<1640:LTRFUA>2.0.CO;2.

——, and D. M. Farmer, 1987: The influence of wind on the underwater sound generated by light rain. *J. Acoust. Soc. Amer.*, **82**, 270–274, https://doi.org/10.1121/1.395563.

——, and H. Medwin, 1995: Underwater sound produced by rainfall: Secondary splashes of aerosols. *J. Acoust. Soc. Amer.*, **97**, 1606–1613, https://doi.org/10.1121/1.412099.

——, C. C. McGlothin, and M. S. Cook, 1993: The underwater sound generated by heavy rainfall. *J. Acoust. Soc. Amer.*, **93**, 3169–3177, https://doi.org/10.1121/1.405701.

Powell, M. D., S. H. Houston, L. R. Amat, and N. Morisseau-Leroy, 1998: The HRD real-time hurricane wind analysis system. *J. Wind Eng. Ind. Aerodyn.*, **77–78**, 53–64, https://doi.org/10.1016/S0167-6105(98)00131-7.

——, and Coauthors, 2010: Reconstruction of Hurricane Katrina's wind fields for storm surge and wave hindcasting. *Ocean Eng.*, **37**, 26–36, https://doi.org/10.1016/j.oceaneng.2009.08.014.

Pun, I. F., Y.-T. Chang, I.-I. Lin, T. Y. Tang, and R.-C. Lien, 2011: Typhoon-ocean interaction in the western North Pacific: Part 2. *Oceanography*, **24** (4), 32–41, https://doi.org/10.5670/oceanog.2011.92.

Risser, M. D., and M. F. Wehner, 2017: Attributable human-induced changes in the likelihood and magnitude of the observed extreme precipitation during Hurricane Harvey. *Geophys. Res. Lett.*, **44**, 12 457–12 464, https://doi.org/10.1002/2017GL075888.

Rogers, R., and E. Uhlhorn, 2008: Observations of the structure and evolution of surface and flight-level wind asymmetries in Hurricane Rita (2005). *Geophys. Res. Lett.*, **35**, L22811, https://doi.org/10.1029/2008GL034774.

Sanford, T. B., J. F. Price, and J. B. Girton, 2011: Upper ocean response to Hurricane Frances (2004) observed by profiling EM-APEX floats. *J. Phys. Oceanogr.*, **41**, 1041–1056, https://doi.org/10.1175/2010JPO4313.1.

Scrimger, J. A., D. J. Evans, G. A. McBean, D. M. Farmer, and B. R. Kerman, 1987: Underwater noise due to rain, hail, and snow. *J. Acoust. Soc. Amer.*, **81**, 79–86, https://doi.org/10.1121/1.394936.

Steffen, J., and M. Bourassa, 2018: Barrier layer development local to tropical cyclones based on Argo float observations. *J. Phys. Oceanogr.*, **48**, 1951–1968, https://doi.org/10.1175/JPO-D-17-0262.1.

——, and ——, 2020: Upper-ocean response to precipitation forcing in an ocean model hindcast of Hurricane Gonzalo. *J. Phys. Oceanogr.*, **50**, 3219–3234, https://doi.org/10.1175/JPO-D-19-0277.1.

Uhlhorn, E. W., and P. G. Black, 2003: Verification of remotely sensed sea surface winds in hurricanes. *J. Atmos. Oceanic Technol.*, **20**, 99–116, https://doi.org/10.1175/1520-0426(2003)020<0099:VORSSS>2.0.CO;2.

——, ——, J. L. Franklin, M. Goodberlet, J. Carswell, and A. S. Goldstein, 2007: Hurricane surface wind measurements from an operational Stepped Frequency Microwave Radiometer. *Mon. Wea. Rev.*, **135**, 3070–3085, https://doi.org/10.1175/MWR3454.1.

Vagle, S., W. G. Large, and D. M. Farmer, 1990: An evaluation of the WOTAN technique of inferring oceanic winds from underwater ambient sound. *J. Atmos. Oceanic Technol.*, **7**, 576–595, https://doi.org/10.1175/1520-0426(1990)007<0576:AEOTWT>2.0.CO;2.

Valle-Levinson, A., M. Olabarrieta, and L. Heilman, 2020: Compound flooding in Houston-Galveston Bay during Hurricane Harvey. *Sci. Total Environ.*, **747**, 141272, https://doi.org/10.1016/j.scitotenv.2020.141272.

van Oldenborgh, G. J., and Coauthors, 2017: Attribution of extreme rainfall from Hurricane Harvey, August 2017. *Environ. Res. Lett.*, **12**, 124009, https://doi.org/10.1088/1748-9326/aa9ef2.

Walsh, E. J., I. PopStefanija, S. Y. Matrosov, J. Zhang, E. Uhlhorn, and B. Klotz, 2014: Airborne rain-rate measurement with a wide-swath radar altimeter. *J. Atmos. Oceanic Technol.*, **31**, 860–875, https://doi.org/10.1175/JTECH-D-13-00111.1.

Willis, R. S., 2010: Analysis of SFMR-derived and satellite-based rain rates over the tropical western North Pacific. Ph.D. thesis, Naval Postgraduate School, 89 pp.

Zhao, Z., E. A. D'Asaro, and J. A. Nystuen, 2014: The sound of tropical cyclones. *J. Phys. Oceanogr.*, **44**, 2763–2778, https://doi.org/10.1175/JPO-D-14-0040.1.

Zhou, X., T. Hara, I. Ginis, E. D'Asaro, J.-Y. Hsu, and B. G. Reichl, 2022: Drag coefficient and its sea state dependence under tropical cyclones. *J. Phys. Oceanogr.*, **52**, 1447–1470, https://doi.org/10.1175/JPO-D-21-0246.1.